




Polarization-independent near-infrared superabsorption in transition metal dichalcogenide Huygens metasurfaces by degenerate critical coupling

Hongju Li ¹, Gangao Wei,¹ Hongmiao Zhou,¹ Haixiao Xiao,¹ Meng Qin,^{1,*} Shengxuan Xia ², and Feng Wu ³

¹*School of Physics, Hefei University of Technology, Hefei, Anhui 230009, China*

²*School of Physics and Electronics, Hunan University, Changsha 410082, China*

³*School of Optoelectronic Engineering, Guangdong Polytechnic Normal University, Guangzhou 510665, China*



(Received 26 December 2021; revised 17 February 2022; accepted 6 April 2022; published 15 April 2022)

Strong near-infrared absorption of light in semiconducting transition metal dichalcogenides (TMDs) is essential for improving the photocarrier extraction efficiency in optoelectronic devices. Here, we numerically demonstrate that an original TMD Huygens metasurface is specifically designed to overcome the 50% absorptance limit of a subwavelength thin film. The unique metasurface comprising a TMD nanodisk array shows evidence of characteristic Mie resonances including electric and magnetic dipoles. By carefully optimizing the aspect ratio of nanodisks, the extraordinary spectral overlapping of orthogonal electric and magnetic dipole resonances is successfully realized and, thus, enables the super-high absorptance up to 87% in a subwavelength-thin ($\approx 0.19\lambda_0$) semiconductor structure by degenerate critical coupling at the wavelength of $\lambda_0 = 903$ nm. All numerical results are confirmed by the temporal coupled-mode theory and again via the multipole decomposition method. Importantly, the near-unity absorptance in this TMD Huygens metasurface by degenerate critical coupling not only is tailored throughout the entire near-infrared region but also is both polarization independent and angle insensitive. The absorptance maintaining $>80\%$ is observed with the incident angle up to $\pm 10^\circ$ at least. Our findings are not only of fundamental interest but could also offer a platform for TMD-based high-speed photodetecting, energy harvesting, and thermal emission.

DOI: [10.1103/PhysRevB.105.165305](https://doi.org/10.1103/PhysRevB.105.165305)

I. INTRODUCTION

Near-infrared semiconductor perfect absorbers [1] have drawn growing research attention, mostly because of their potential applications for high-efficiency optoelectronic devices, ranging from sensors [2], photodetectors [3] to thermal emitters [4], and spatial light modulators [5]. Importantly, strong absorption of light in the layer of semiconductors [6,7] is beneficial for reducing the photocarrier extraction time, enhancing the photocarrier extraction efficiency, suppressing dark currents, and developing ultrafast optoelectronic devices with low material cost. Over the past two decades, advances in synthesis, processing, and nanofabrication of low-dimensional materials have allowed significant progress toward flexible, ultra-thin semiconductor layers [8,9] and even semiconductors with only one atom of thickness [10,11]. Specifically, the emergence of two-dimensional transition metal dichalcogenide (TMD) atomic layers with large direct bandgap and low dark current has offered a class of high-radiative-efficiency semiconductors that can be synthesized in ultra-thin form [12]. However, owing to the atomically thin nature which is extensively mismatched with optical wavelengths, the single-pass absorptance in freestanding monolayers of TMDs (such as MoS_2) is only $\sim 10\text{--}20\%$ from visible to near-infrared regions [13]. Although the absorptance is considerably high for semiconductor film with a thickness < 1 nm, it is still insufficient for high-performance optoelec-

tronic devices [14]. To expand the practical applications of TMD semiconductors, further enhancement of the absorption of light is urgent. The strong absorption of light in TMD layers will generate more electron-hole pairs. When TMD layers contact a metallic electrode, such as the graphene monolayer, a depletion region called the Schottky junction often forms at the graphene-TMD interface due to the difference of their work functions, thereby enabling a built-in electric field. Based on the internal potential, a large crowd of photoinduced electron-hole pairs in TMD layers will be separated at the graphene-TMD interface. Holes flow to graphene, whereas electrons are trapped in TMD, acting as a local gate. Under the applied bias, photocarriers transport rapidly in the graphene layer, resulting in the significant enhancement of the photoelectric efficiency [15].

So far, many efforts have been dedicated to boosting the absorption of light in TMD layers from visible to near-infrared regions, and most solutions are associated with additionally introduced metallic rear surfaces [16,17] or nanostructured metallic particles supporting localized surface plasmon resonances [18,19]. For TMD-on-metal absorbers, metallic rear surfaces are commonly interpreted as simple ray optical specular reflectors. For plasmon-based TMD absorbers, the usual noble metallic nanoparticles, such as silver nanodisks [20], gold nanorods [21], and silver cubes [22], have been proposed to integrate with TMD monolayers. The excitation of localized plasmon resonances on metallic nanoparticles enables tight light trapping and strong electromagnetic field enhancement and thereby substantially boosts the light-matter interaction in neighboring layers of TMD semiconductors.

*qinm@hfut.edu.cn

However, for these TMD semiconductor absorbers with the aid of metals, on the one hand, the metallic rear surface gives rise to strong reflection outside the absorptance band and thus enables the investigated absorbers to lose the desired feature of out-of-band transparency. On the other hand, once metals are involved, the incident light is significantly absorbed to generate heat in metals, instead of photocarriers generated in TMD semiconductors. These drawbacks undoubtedly are unfavorable for ultrafast optoelectronic devices. In this circumstance, the concept of all-TMD semiconductor absorbers is highly desired.

Interestingly, owing to the strong in-plane bonding of transition metals to chalcogens and the low dielectric screening as well as the highly confined exciton wave functions, semiconducting TMDs possess high refractive indices and extinction coefficients at visible and near-infrared regions [23]. Therefore, to boost the absorption in TMD semiconductors without the aid of additional metallic structures, the thicker TMD layer is necessary. The above-gap absorptance in a freestanding bulk TMD film is limited to a maximum of $\sim 40\%$. Owing to the large refractive index mismatch between TMD crystals and the background, a large fraction (50–60%) of incident light is reflected from the TMD surface [24]. Thus, even though we increase the thickness of TMD layers, we cannot break the 50% absorptance limit of nonmagnetic subwavelength film in principle [25]. To overcome this limitation, nanopatterned TMD metasurfaces with high refractive indices and moderate intrinsic losses simultaneously [26] are feasible. Nanopatterned TMD metasurfaces with high refractive indices are well known to support Mie resonances [27–29], such as the typical electric dipole (ED) and magnetic dipole (MD) modes originating from displacement currents. The individual ED or MD resonance with strong near-field enhancement can boost the absorption of light in TMD semiconductors, even approaching the 50% absorptance limit of an ultra-thin nanostructure array by critical coupling [30]. More importantly, once the orthogonal ED and MD resonances are simultaneously supported on a TMD metasurface, the realization of spectral superposition of ED and MD resonances is possible (namely, the so-called Huygens metasurface forms [31–33]). The combination of TMD Huygens metasurfaces and the degenerate critical coupling [34,35] will open an opportunity to break the 50% absorptance limit of an ultra-thin nanostructure array and thereby allow the perfect absorptance in TMD semiconductors in theory. Reports of the perfect absorptance of light in all-TMD metasurfaces by degenerate critical coupling are lacking.

Herein, we investigate a TMD Huygens metasurface consisting of a periodic tungsten disulfide (WS_2) nanodisk array both numerically and theoretically. The results from finite-difference time-domain (FDTD) simulations exhibit that spectral overlapping of orthogonal ED and MD resonances is realized by carefully optimizing the aspect ratio of WS_2 nanodisks. The super-high absorptance up to 87% is successfully achieved in the subwavelength-thin ($\approx 0.19 \lambda$) TMD semiconductor by degenerate critical coupling at the crossing of orthogonal ED and MD resonances. The typical temporal coupled-mode theory (TCMT) and the multipole decomposition method are used for illustrating the underlying physics. All FDTD simulations are consistent with the

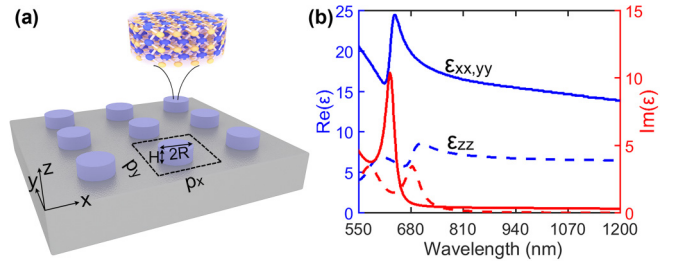


FIG. 1. (a) Schematic of the proposed all-transition metal dichalcogenide (TMD) Huygens metasurface with detailed structural description. (b) In-plane ($\epsilon_{xx,yy}$) and out-of-plane (ϵ_{zz}) dielectric functions of bulk WS_2 .

theoretical calculations. Intriguingly, the near-unity absorptance in this TMD Huygens metasurface by degenerate critical coupling not only can be tailored throughout the entire near-infrared region but also is both polarization independent and angle insensitive. Accompanied by the perfect absorptance in all-TMD semiconductors, our results undoubtedly establish TMDs for optoelectronic device applications ranging from high-speed photodetecting, energy harvesting to thermal emission, and nonlinear optics.

II. STRUCTURE AND PRINCIPLE

Figure 1(a) depicts the proposed all-TMD metasurface comprising a periodic WS_2 nanodisk array on a low-index dielectric substrate. Here, R and H denote the radius and height of WS_2 nanodisks, respectively, and p_x and p_y represent periods along the x and y directions, respectively. Certainly, our observations are not unique to WS_2 and can be further generalized to other TMDs. The anisotropic dielectric functions of bulk WS_2 [27] are shown in Fig. 1(b). As indicated by the blue solid curve, the in-plane refractive index calculated by $n_{xx,yy} = \sqrt{\epsilon_{xx,yy}} > 4$ is observed from the visible to near-infrared regions and thus is significantly higher than most conventional semiconductor materials, such as silicon with a refractive index of 3.45 and titanium dioxide with a refractive index of 2.5. The high refractive index will allow nanopatterned WS_2 nanodisks to support specific geometrical resonances with tight confinement of light, such as classical Mie resonances. In addition, as indicated by the red solid curve, almost the same extinction coefficients determined by the imaginary parts of permittivity occur at the entire near-infrared region from 700 to 1200 nm. The moderate intrinsic loss plays a dominant role in realizing strong absorption of light in semiconductor nanostructures [36] since it is a key factor to balance the inevitable radiative loss of Mie resonances. The prominent peak at the wavelength of $\lambda = 615$ nm is attributed to A-exciton absorption due to the interband electronic transition at the K valley of a hexagonal Brillouin zone [37]. The relatively low permittivity in the out-of-plane components marked by dash curves is attributed to the van der Waals nature of the layer interaction. Importantly, when a plane wave with the electric field (\mathbf{E}) in the x - y plane irradiates a WS_2 metasurface with a thickness much smaller than optical wavelengths, the in-plane permittivity will play a main role in the corresponding geometrical resonances. For

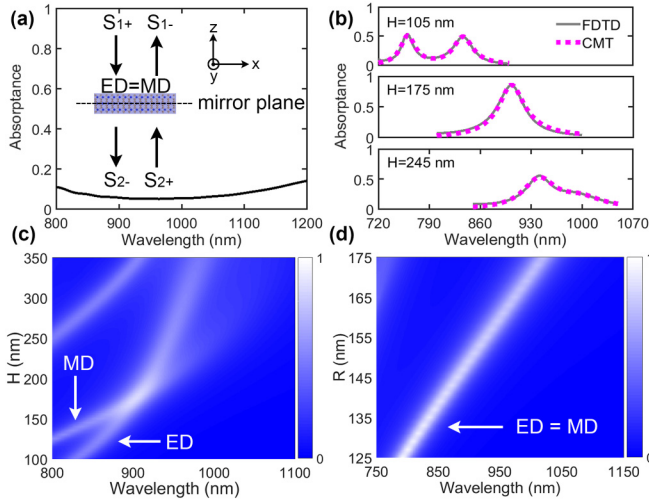


FIG. 2. (a) Absorbance spectrum of a WS_2 film with a thickness of 175 nm. The inset describes the schematic of temporal coupled-mode theory (TCMT) used for our proposed mirror-symmetric two-port system. The x - z cross-section of a unit cell is presented. (b) Absorbance spectra of WS_2 metasurfaces for different heights. (c) Color-coded absorbance spectra as a function of heights with unchanged radii of $R = 150$ nm. (d) Evolution of absorbance spectra on the radius R with a fixed aspect ratio of $2R/H = \frac{12}{7}$.

simplicity, a WS_2 metasurface embedded in vacuum is considered. We can access the system from both sides, so each face of the WS_2 nanodisk acts as a port. The system possesses a mirror plane at $z = 0$ as represented by the black dashed line in the inset of Fig. 2(a). Therefore, a mirror-symmetric two-port system with respect to the mirror plane forms. Mie resonances including ED and MD modes are well known to be supported by a WS_2 nanodisk. The electric field of ED resonances is always symmetric with respect to the mirror plane of nanodisks. The ED resonance thus is defined as an even eigenmode, whereas the MD resonance is antisymmetric and acts as an odd eigenmode. The structure we proposed hence behaves as a mirror-symmetric two-port system with two orthogonal eigenmodes simultaneously. Certainly, when the same transparent substrate and superstrate with a low refractive index are introduced simultaneously, the system with mirror symmetry will be maintained, and thus, the underlying physics is unchanged. The reciprocal resonant system permits the use of typical TCMT [38–40] to uncover the underlying physics.

III. TCMT FOR TOTAL ABSORPTANCE

The schematic of TCMT is presented in the inset of Fig. 2(a). The dynamic equations for eigenmode amplitudes and the relationship between input and output waves are respectively written as [38]

$$\frac{d\mathbf{a}}{dt} = (-j\mathbf{\Omega} - \mathbf{\Gamma})\mathbf{a} + \mathbf{D}^T \mathbf{S}_+, \quad (1)$$

$$\mathbf{S}_- = \mathbf{C}\mathbf{S}_+ + \mathbf{D}\mathbf{a}, \quad (2)$$

where j stands for the imaginary unit. Here, $\mathbf{a} = [a_1 a_2]^T$ is the normalized resonant amplitudes vector, and $a_{i=1,2}$ represent

ED and MD modes, respectively. The stored energy for each mode is determined by $W_i = a_i^* a_i = |a_i|^2$ [41]. Here, $\mathbf{S}_+ = [S_{1+} 0]^T$ stands for input waves only from port 1, and $|S_{1+}|^2$ is the input power. A similar term is for output waves denoted by $\mathbf{S}_- = [S_{1-} S_{2-}]^T$. The matrices $\mathbf{\Omega}$ and $\mathbf{\Gamma}$ denote the resonant frequencies and decay rates of eigenmodes, respectively. They are expressed as

$$\mathbf{\Omega} = \begin{bmatrix} \omega_1 & 0 \\ 0 & \omega_2 \end{bmatrix}, \quad (3)$$

$$\mathbf{\Gamma} = \begin{bmatrix} \gamma_1 + \delta_1 & \gamma_c \\ \gamma_c^* & \gamma_2 + \delta_2 \end{bmatrix}. \quad (4)$$

Here, $\omega_{i=1,2}$ represent the resonant frequencies of ED and MD modes, respectively. The corresponding $\gamma_{i=1,2}$ and $\delta_{i=1,2}$ denote the radiation rates and intrinsic material loss rates for each eigenmode, respectively, and γ_c defines the coupling coefficient between ED and MD modes. Here, \mathbf{C} is the scattering matrix of input and output waves in the absence of resonant modes and, thus, represents the coupling between input and output waves in a direct nonresonant pathway from port 1 to port 2. It is in general expressed as

$$\mathbf{C} = \begin{bmatrix} 0 & 1 \\ 1 & 0 \end{bmatrix}. \quad (5)$$

Here, \mathbf{D} is the coupling matrix between eigenmodes and input waves as well as output waves and is expressed by a 2×2 matrix:

$$\mathbf{D} = \begin{bmatrix} d_{11} & d_{12} \\ d_{21} & d_{22} \end{bmatrix}. \quad (6)$$

Based on the energy conservation where we consider the external incident waves are absent ($\mathbf{S}_+ = [0 0]^T$) and thus the decaying of resonant amplitudes is due entirely to the creation of outgoing waves, we have

$$\mathbf{D}^\dagger \mathbf{D} = 2 \begin{bmatrix} \gamma_1 & \gamma_c \\ \gamma_c^* & \gamma_2 \end{bmatrix}. \quad (7)$$

Based on the time-reversal symmetry, we have

$$\mathbf{C}\mathbf{D}^* = -\mathbf{D}. \quad (8)$$

Applying Eq. (6) to Eqs. (7) and (8), and concurrently considering the system with mirror symmetry, we get

$$|d_{11}| = |d_{21}| = \sqrt{\gamma_1}, \quad |d_{12}| = |d_{22}| = \sqrt{\gamma_2}. \quad (9)$$

Therefore, the elements of matrix \mathbf{D} are obtained as

$$\mathbf{D} = \begin{bmatrix} \sqrt{\gamma_1} e^{-j\theta_{11}} & \sqrt{\gamma_2} e^{-j\theta_{12}} \\ \sqrt{\gamma_1} e^{-j\theta_{21}} & \sqrt{\gamma_2} e^{-j\theta_{22}} \end{bmatrix}. \quad (10)$$

Here, θ_{ij} (i or $j = 1, 2$) is the phase angle of elements of the coupling matrix \mathbf{D} . Because the system has mirror plane symmetry, and the ED mode decays symmetrically while the MD mode decays antisymmetrically with respect to the mirror plane of WS_2 nanodisks, we have $\theta_{11} = \theta_{21}$ and $\theta_{12} = \theta_{22} + \pi$. Meanwhile, when the rewritten matrix \mathbf{D} in Eq. (10) is plugged into the equation of energy conservation, we also have

$$\exp(j\theta_{12} - j\theta_{11}) + \exp(j\theta_{22} - j\theta_{21}) = 2 \frac{\gamma_c}{\sqrt{\gamma_1 \gamma_2}}. \quad (11)$$

In addition, the time-reversal symmetry suggests $\mathbf{CD}^* = -\mathbf{D}$, and then we have $\theta_{11} = \theta_{21} = \pi/2$, $\theta_{12} = \pi$, $\theta_{22} = 0$. Equation (11) is evolved into

$$\exp(j\theta_{12} - j\theta_{11}) = -\exp(j\theta_{22} - j\theta_{21}). \quad (12)$$

Finally, $\gamma_c = 0$ is obtained, and the matrix \mathbf{D} is expressed as

$$\mathbf{D} = \begin{bmatrix} -j\sqrt{\gamma_1} & -\sqrt{\gamma_2} \\ -j\sqrt{\gamma_1} & \sqrt{\gamma_2} \end{bmatrix}. \quad (13)$$

Using the frequency domain $\exp(-j\omega t)$ to isolate resonant amplitudes of eigenmodes, the elements of matrix \mathbf{a} are expressed as

$$a_1 = \frac{-j\sqrt{\gamma_1}S_{1+}}{-j(\omega - \omega_1) + \gamma_1 + \delta_1},$$

$$a_2 = \frac{-\sqrt{\gamma_2}S_{1+}}{-j(\omega - \omega_2) + \gamma_2 + \delta_2}. \quad (14)$$

Here, $\gamma_c = 0$ denotes that there is no coupling between ED and MD modes. Thus, the two eigenmodes are independent. Because the decay rate induced by the intrinsic material loss for $W_i = a_i^*a_i = |a_i|^2$ is $2\delta_i$, the dissipation loss power in each resonance mode is calculated by

$$P_{d,i} = 2\delta_i W_i = 2\delta_i |a_i|^2 = \frac{2\delta_i \gamma_i |S_{1+}|^2}{(\omega - \omega_i)^2 + (\gamma_i + \delta_i)^2}. \quad (15)$$

The absorptance resulting from each eigenmode resonance is normalized to input power $|S_{1+}|^2$ and thereby is described by

$$A_i = \frac{P_{d,i}}{|S_{1+}|^2} = \frac{2\delta_i \gamma_i}{(\omega - \omega_i)^2 + (\gamma_i + \delta_i)^2}. \quad (16)$$

Equation (16) suggests that the maximum absorptance of individual ED or MD resonances is 50%, when the critical coupling ($\gamma_i = \delta_i$) is satisfied. The total absorptance of the metasurface system thus is the sum of two independent absorptance in orthogonal eigenmodes (ED and MD) and is given by

$$A = \sum_{i=1}^2 \frac{2\delta_i \gamma_i}{(\omega - \omega_i)^2 + (\gamma_i + \delta_i)^2}. \quad (17)$$

Equation (17) indicates that 100% absorptance of light by the WS_2 metasurface is possible, provided that the independent critical coupling ($\gamma_i = \delta_i$) occurs at the crossing of two orthogonal eigenmodes simultaneously (namely, the appearance of degenerate critical coupling). Meanwhile, the occurrence of spectral superposition of orthogonal ED and MD resonances shows evidence of a WS_2 Huygens metasurface.

IV. SIMULATION AND DISCUSSION

To verify the prediction from TCMT, a series of FDTD numerical simulations is performed to investigate the absorptance property of a freestanding WS_2 Huygens metasurface with $H = 175$ nm and $R = 150$ nm. The periods in x and y directions are assumed to be $p_x = 720$ nm and $p_y = 640$ nm,

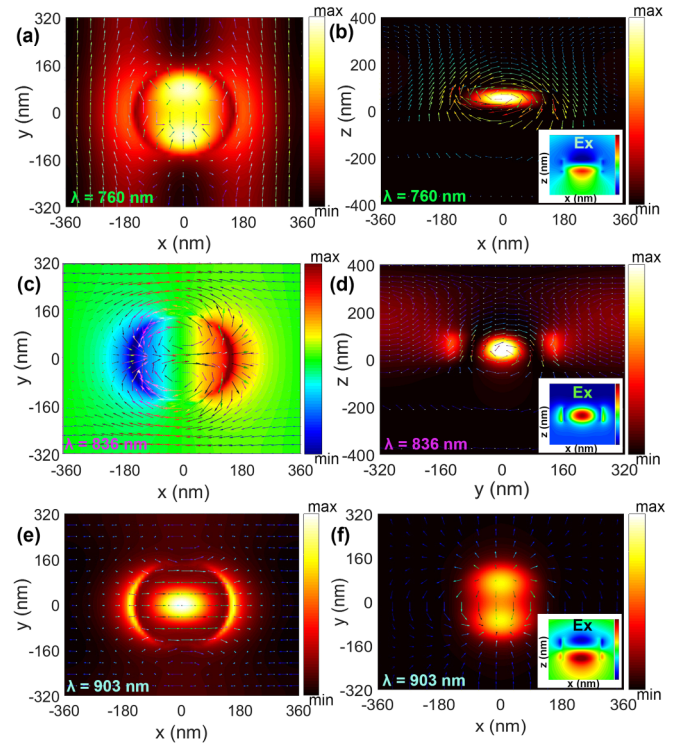


FIG. 3. (a) Electric field $|E|^2$ distributions of x - y cross-section at $\lambda = 760$ nm. The arrows indicate the magnetic field vector. (b) Magnetic field $|H|^2$ distributions of x - z cross-section at $\lambda = 760$ nm. The arrows indicate the electric field vector. (c) Electric field E_z distributions of x - y cross-section at $\lambda = 836$ nm. The arrows indicate the electric field vector. (d) Electric field $|E|^2$ distributions of y - z cross-section at $\lambda = 836$ nm. The arrows indicate the magnetic field vector. (e) Electric field $|E|^2$ distributions of x - y cross-section at $\lambda = 903$ nm. The arrows indicate the electric field vector. (f) Magnetic field $|H|^2$ distributions of x - y cross-section at $\lambda = 903$ nm. The arrows indicate the magnetic field vector. The insets in (b), (d), and (f) show electric field E_x distributions of x - z cross-section at $\lambda = 760$, 836, and 903 nm, respectively. $H = 105$ nm is for (a)–(d), and $H = 175$ nm is for (e) and (f).

respectively. In the implementation, periodic boundary conditions are applied in the x and y directions. Perfectly matched layer absorption conditions are utilized for the z direction. The normally incident plane wave is with the electrical polarization along the x direction. The polarization angle is defined as the angle between the x axis and the incident electric field. The mesh size is chosen as 2 nm for good convergence of numerical simulations. Simulated results are presented in Fig. 2. As a comparison, the absorptance of a uniform WS_2 film with a thickness of 175 nm is also provided and marked by the black curve in Fig. 2(a). The absorptance $< 15\%$ in the entire near-infrared region from 800 to 1200 nm is witnessed. The low absorptance without obvious peaks can be well understood. There are no geometrical resonances on the infinite WS_2 film with thickness much smaller than optical wavelengths, and thus, the absorptance is determined only by the imaginary parts of the permittivity of WS_2 . The result is in accord with the 50% absorptance limit of a subwavelength-thin film [34]. On the contrary, once the WS_2 metasurface is constructed, Mie resonances, such as ED and MD, will be excited on

the periodic WS₂ nanodisks with high refractive index due to the diffraction effect. Each Mie resonance will allow the WS₂ metasurface to realize maximum absorptance of 50% in principle, according to Eq. (16).

Figure 2(b) shows absorptance spectra of WS₂ metasurfaces with $H = 105, 175,$ and 245 nm, respectively. Comparison of three curves suggests that each separated resonance indeed cannot break the 50% absorptance limit, as predicted by Eq. (16). Two separated 50% absorptance peaks occur at $\lambda = 760$ and 836 nm, respectively, when the thickness is $H = 105$ nm. At $H = 175$ nm, only one absorptance peak is observed at $\lambda = 903$ nm, and the super-high absorptance up to 87% yields. The 50% absorptance limit thus is broken. The single near-unity absorptance could be attributed to the superposition of two original separated absorptance peaks. More favorable evidence for the superposition of two resonances at $H = 175$ nm can be found in Fig. 2(c), where the color-coded absorptance spectra as a function of H are presented. As the height H increases, two eigenmodes tend to exhibit a redshift simultaneously. However, one eigenmode is more sensitive to the height H and thereby results in a merge of resonant frequencies at $H = 175$ nm. Away from the crossing, each resonance has a maximum absorptance of $\sim 50\%$. While at the crossing of two eigenmodes, the absorptance of each resonance sums, and thus, the absorptance up to 87% is achieved. The results are consistent with the prediction from the Eq. (17), where the 50% absorptance limit is overcome by degenerate critical coupling.

To provide an explicit understanding of the superposition of eigenmodes with the height increasing, electromagnetic field distributions of each resonance are presented in Fig. 3. Away from the degeneracy, such as at the $H = 105$ nm, the absorptance peaks of two eigenmodes occur at wavelengths of 760 and 836 nm, respectively. For the resonance at $\lambda = 760$ nm, the electric field distributions at the x - y cross-section

and magnetic field distributions at the x - z cross-section are shown in Figs. 3(a) and 3(b), respectively. The displacement current loop in the x - z cross-section suggests that the MD resonance along the y direction yields. Hence, the antisymmetric electric field distributions with respect to the mirror plane of WS₂ nanodisks occurs, as seen in the inset of Fig. 3(b). As expected, the MD resonance behaves as an odd eigenmode in this mirror-symmetric two-port system. For the resonance at $\lambda = 836$ nm with field distributions shown in Figs. 3(c) and 3(d), the electric field along the x direction concurrently with the circular magnetic field in the y - z cross-section indicates that the ED resonance along the x direction forms. The symmetric electric field distributions with respect to the mirror plane of WS₂ nanodisks occurs, as seen in the inset of Fig. 3(d). Thus, the ED resonance is well treated as an even eigenmode. Importantly, as described in Figs. 3(e) and 3(f) as well as the inset, the electric field and magnetic field distributions of the x - y cross-section at the crossing of $\lambda = 903$ nm indeed reveal the signature of superposition of MD and ED resonances, which means the realization of an original WS₂ Huygens metasurface. The orthogonal ED and MD resonances with respect to the mirror plane of WS₂ nanodisks are decoupled at the crossing, and thus, the degeneracy occurs.

Furthermore, the Cartesian multipole decomposition method [42–44] allows us to gain a quantitative understanding of the eigenmodes of the investigated WS₂ metasurface. The induced multipole moments are calculated by integrating the displacement current density $\vec{J}(\vec{r})$ within a unit cell of the periodic WS₂ metasurface. The expressions used for calculating the five leading multipole moments including the ED moment (\vec{P}), the MD moment (\vec{M}), the toroidal dipole (TD) moment (\vec{T}), the electric quadrupole (EQ) moment [$Q_{\alpha\beta}^{(e)}$], and the magnetic quadrupole (MQ) moment [$Q_{\alpha\beta}^{(m)}$] are shown as the following [42]:

$$\vec{P} = \frac{1}{i\omega} \int \vec{J} d^3r, \quad (18)$$

$$\vec{M} = \frac{1}{2c} \int (\vec{r} \times \vec{J}) d^3r, \quad (19)$$

$$\vec{T} = \frac{1}{10c} \int [(\vec{r} \cdot \vec{J})\vec{r} - 2r^2\vec{J}] d^3r, \quad (20)$$

$$\left. \begin{aligned} Q_{\alpha\beta}^{(e)} &= \frac{1}{i\omega} \int [r_\alpha J_\beta + r_\beta J_\alpha - \frac{2}{3}(\vec{r} \cdot \vec{J})] d^3r \\ Q_{\alpha\beta}^{(m)} &= \frac{1}{3c} \int [(\vec{r} \times \vec{J})_\alpha r_\beta + (\vec{r} \times \vec{J})_\beta r_\alpha] d^3r \end{aligned} \right\} \alpha, \beta = x, y, z. \quad (21)$$

Here, c and ω are the speed and angular frequency of light in vacuum, respectively, and \vec{r} is the distance vector from the origin to point (x, y, z) in a Cartesian coordinate system. Then the sum of far-field scattered energy from multipole excitations is calculated by

$$\begin{aligned} I_{\text{scattering}} &= I_P + I_M + I_T + I_{Q^{(e)}} + I_{Q^{(m)}} \\ &= \frac{2\omega^4}{3c^3} |\vec{P}|^2 + \frac{2\omega^4}{3c^3} |\vec{M}|^2 + \frac{2\omega^6}{3c^5} |\vec{T}|^2 \end{aligned}$$

$$+ \frac{\omega^6}{5c^5} \sum |Q_{\alpha\beta}^{(e)}|^2 + \frac{\omega^6}{40c^5} \sum |Q_{\alpha\beta}^{(m)}|^2. \quad (22)$$

In Fig. 4, the results of the multipole decomposition are expressed in logarithmic coordinates. The scattered energy as a function of wavelengths for WS₂ metasurfaces with $H = 105$ and 175 nm are shown in Figs. 4(a) and 4(b), respectively. As indicated by the shaded areas in Fig. 4(a), it is obvious that the eigenmode at $\lambda = 760$ nm is dominated by the MD resonance,

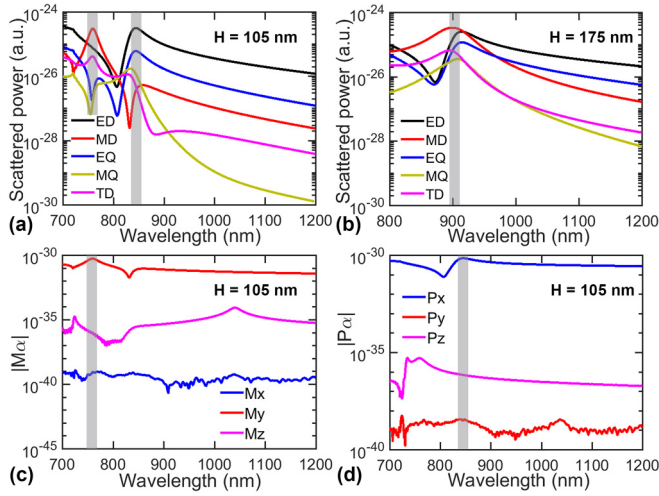


FIG. 4. Scattered energy of five leading multipoles of WS_2 metasurfaces with (a) $H = 105$ nm and (b) 175 nm. (c) Magnetic dipole (MD) moment and (d) electric dipole (ED) moment of a WS_2 metasurface with $H = 105$ nm.

and the eigenmode at $\lambda = 836$ nm is dominated by the ED resonance. Meanwhile, as anticipated, the superposition of absorptance peaks at $\lambda = 903$ nm is determined by MD and ED resonances simultaneously, as seen in the shaded area of Fig. 4(b). It is further worth noting that the calculated MD moment (\vec{M}) and ED moment (\vec{P}) for the WS_2 metasurface with $H = 105$ nm are demonstrated in Figs. 4(c) and 4(d), respectively. We do observe the MD resonance along the y direction and the ED resonance along the x direction. With respect to the mirror plane of WS_2 nanodisks, two orthogonal eigenmodes are obtained. Thus, the near-unity absorptance at $H = 175$ nm can be attributed to the degenerate critical coupling, as described by the TCMT. The TCMT-fitted absorptance spectra by using Eq. (17) with four parameters (the γ_1, δ_1 for the ED mode, and γ_2, δ_2 for the MD mode) are marked by purple dotted curves in Fig. 2(b). In fact, it is uncertain to distinguish γ_1, δ_1 and γ_2, δ_2 . It is because $\gamma_{i=1,2}$ and $\delta_{i=1,2}$ play the same role in Eq. (17) for fitting the FDTD absorptance spectrum, when we do not consider their physical meanings. However, the greater height H means a larger intrinsic material loss rate δ_1 for the ED mode with the electric field strongly confined within WS_2 nanodisks. Hence, a monotonic variation of δ_1 with the height H is confirmed for the ED mode. In addition, we can approximately estimate γ_1 and γ_2 according to the full width at half maximum of scattering spectra obtained by using the Cartesian multipole decomposition method. Here, $\gamma_1 > \gamma_2$ at $H = 105$ nm, $\gamma_1 < \gamma_2$ at $H = 175$ nm, and $\gamma_1 < \gamma_2$ at $H = 245$ nm thus are obtained. The four fitted parameters are finally presented on Table I. The results of degenerate coupled mode theory are in excellent agreement with FDTD simulated absorptance spectra. A notable observation in our theoretical findings is that the imperfect absorptance ($87 < 100\%$) at $H = 175$ nm is primarily attributed to the imperfect critical coupling ($\gamma_2 \neq \delta_2$) of the MD (odd eigenmode) resonance.

Like the change in heights with a fixed radius [as shown in Fig. 2(c)], the individual change in radii with a unchanged height will also give rise to a crossing of ED and MD

TABLE I. The TCMT-fitted parameters for absorptance spectra in Fig. 2(b).

H (nm)	γ_1 (Hz)	δ_1 (Hz)	γ_2 (Hz)	δ_2 (Hz)
105	2.62×10^{13}	1.77×10^{13}	2.02×10^{13}	2.02×10^{13}
175	2.11×10^{13}	2.11×10^{13}	5.36×10^{13}	1.69×10^{13}
245	3.12×10^{13}	2.69×10^{13}	5.97×10^{13}	5.89×10^{12}

resonances because ED and MD resonances with opposite symmetry exhibit more sensitivity to heights and radii of WS_2 nanodisks, respectively. Interestingly, the colormap shown in Fig. 2(c) suggests degenerate critical coupling occurs at a WS_2 metasurface with the aspect ratio of $2R/H = \frac{12}{7}$. Therefore, the crossing of ED and MD resonances on WS_2 nanodisks can be fulfilled at other wavelengths, when we vary the radius but with a fixed aspect ratio of $2R/H = \frac{12}{7}$. In other words, the near-unity absorptance in this WS_2 Huygens metasurface by degenerate critical coupling can be tailored throughout the entire near-infrared region. The evolution of absorptance spectra on the radius but with a fixed aspect ratio is shown in Fig. 2(d). As expected, the dynamic tunability of the near-unity absorptance peak is observed, which will enable the TMDs for high-efficiency optoelectronic device applications at the entire near-infrared region from 800 to 1200 nm. It should also be pointed out that the interaction between WS_2 nanodisks in different unit cells depends on the period of metasurfaces. We consider the effect of periods here. The evolution of absorptance spectra on periods is shown in Figs. 5(a) and 5(b). The comparison of two colormaps demonstrates that the period p_x has a weak effect on the MD resonance along the y direction, whereas p_y has a weak effect on the ED resonance along the x direction. Hence, to ensure the maximum absorptance induced by degenerate critical coupling at the crossing of ED and MD resonances, careful geometry optimization is necessary.

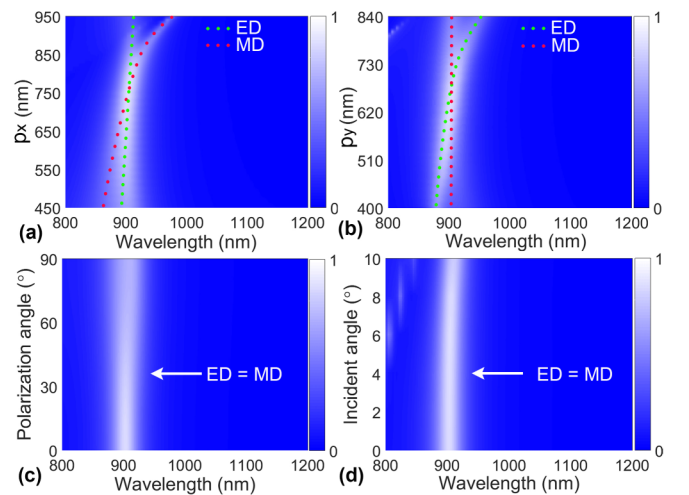


FIG. 5. Color-coded absorptance spectra as a function of (a) p_x and (b) p_y . The red and green dotted curves guide the changes of magnetic dipole (MD) and electric dipole (ED) resonant peaks. Evolution of absorptance spectra on (c) polarization angles and (d) incident angles. Other simulated details are identical to those used in Fig. 3(e), except the variable parameter in each subfigure.

Thus far, our discussion concerning near-unity absorptance of a WS_2 metasurface by degenerate critical coupling has been focused on normal incidence illumination. We further investigate the evolution of near-unity absorptance by degenerate critical coupling on polarization angles and incident angles, respectively. The optimized geometric parameters with $H = 175$ nm and $R = 150$ nm are used for achieving the crossing of ED and MD resonances at the wavelength of $\lambda = 903$ nm. With the fixed geometry structure, the absorptance spectra at varying polarization angles and incident angles are shown in Figs. 5(c) and 5(d), respectively. The near-unity absorptance at $\lambda = 903$ nm is observed to be polarization-independent, as seen in Fig. 5(c), due to the axial symmetry of WS_2 nanodisks. Intriguingly, under the oblique incidence, the results in Fig. 5(d) show that the high absorptance ($>80\%$) originating from the overlapping of ED and MD resonances at $\lambda = 903$ nm can be maintained within $\pm 10^\circ$ at least. Both the outstanding polarization-independent and angle-insensitive features undoubtedly are beneficial for the practical applications of TMD Huygens metasurfaces predominately studied in this paper.

V. CONCLUSIONS

In summary, we have both numerically and theoretically demonstrated that a unique TMD Huygens metasurface is

deterministically designed to overcome the 50% absorptance limit of a thin film and to realize near-unity absorptance in the subwavelength-thin ($\approx 0.19 \lambda$) semiconducting nanostructure. Simulated results exhibit that the realization of this all-TMD semiconductor absorber is attributed to degenerate critical coupling at the crossing of orthogonal ED and MD resonances on the mirror-symmetric system. All numerical results are in excellent agreement with the theoretical calculations from TCMT and the multipole decomposition method. Importantly, the super-high absorptance in TMD semiconductors by degenerate critical coupling not only can be tailored throughout the entire near-infrared region via altering geometric parameters of Huygens metasurfaces but also is both polarization independent and angle insensitive. Our observations undoubtedly lay the foundation toward a material platform for TMD-based high-efficiency photodetecting, energy harvesting, and thermal emission.

ACKNOWLEDGMENTS

This paper is supported by the National Natural Science Foundation of China (Grants No. 61805064 and No. 12104105), the Fundamental Research Funds for the Central Universities of China (Grants No. PA2021KCPY0052, No. JZ2021HGQA0259, and No. JZ2021HGTA0143), and the Start-up Funding of Guangdong Polytechnic Normal University (Grant No. 2021SDKYA033).

-
- [1] C. M. Watts, X. Liu, and W. J. Padilla, Metamaterial electromagnetic wave absorbers, *Adv. Mater.* **24**, OP98 (2012).
 - [2] W. Xu, L. Xie, and Y. Ying, Mechanisms and applications of terahertz metamaterial sensing: A review, *Nanoscale* **9**, 13864 (2017).
 - [3] Z. Chen, Y. Weng, J. Liu, N. Guo, Y. Yu, and L. Xiao, Dual-band perfect absorber for a mid-infrared photodetector based on a dielectric metal metasurface, *Photonics Res.* **9**, 27 (2021).
 - [4] M. Diem, T. Koschny, and C. M. Soukoulis, Wide-angle perfect absorber/thermal emitter in the terahertz regime, *Phys. Rev. B* **79**, 033101 (2009).
 - [5] S. G. C. Carrillo, G. R. Nash, H. Hayat, M. J. Cryan, M. Klemm, H. Bhaskaran, and C. D. Wright, Design of practicable phase-change metadevices for near-infrared absorber and modulator applications, *Opt. Express* **24**, 13563 (2016).
 - [6] N. O. Lank, R. Verre, P. Johansson, and M. Kall, Large-scale silicon nanophotonic metasurfaces with polarization independent near-perfect absorption, *Nano Lett.* **17**, 3054 (2017).
 - [7] P. Tang, G. Liu, X. Liu, G. Fu, Z. Liu, and J. Wang, Plasmonic wavy surface for ultrathin semiconductor black absorbers, *Opt. Express* **28**, 27764 (2020).
 - [8] D. Jariwala, A. R. Davoyan, G. Tagliabue, M. C. Sherrott, J. Wong, and H. A. Atwater, Near-unity absorption in van der Waals semiconductors for ultrathin optoelectronics, *Nano Lett.* **16**, 5482 (2016).
 - [9] Y. Chen, J. Liu, M. Zeng, F. Lu, T. Lv, Y. Chang, H. Lan, B. Wei, R. Sun, J. Gao, Z. Wang, and L. Fu, Universal growth of ultra-thin III-V semiconductor single crystals, *Nat. Commun.* **11**, 3979 (2020).
 - [10] K. S. Novoselov, O. A. Mishchenko, O. A. Carvalho, and A. C. Neto, 2D materials and van der Waals heterostructures, *Science* **353**, aac9439 (2016).
 - [11] Z. Lin, Y. Liu, U. Halim, M. Ding, Y. Liu, Y. Wang, C. Jia, P. Chen, X. Duan, C. Wang, F. Song, M. Li, C. Wan, Y. Huang, and X. Duan, Solution-processable 2D semiconductors for high-performance large-area electronics, *Nature (London)* **562**, 254 (2018).
 - [12] A. K. Geim and I. V. Grigorieva, Van der Waals heterostructures, *Nature (London)* **499**, 419 (2013).
 - [13] J. T. Liu, T. B. Wang, X. J. Li, and N. H. Liu, Enhanced absorption of monolayer MoS_2 with resonant back reflector, *J. Appl. Phys.* **115**, 193511 (2014).
 - [14] O. Lopez-Sanchez, D. Lembke, M. Kayci, A. Radenovic, and A. Kis, Ultrasensitive photodetectors based on monolayer MoS_2 , *Nat. Nanotechnol.* **8**, 497 (2013).
 - [15] R. Liu, F. Wang, L. Liu, X. He, J. Chen, Y. Li, and T. Zhai, Band alignment engineering in two-dimensional transition metal dichalcogenide-based heterostructures for photodetectors, *Small Struct.* **2**, 2000136 (2020).
 - [16] W. Wang, A. Klots, Y. Yang, W. Li, I. I. Kravchenko, D. P. Briggs, K. I. Bolotin, and J. Valentine, Enhanced absorption in two-dimensional materials via Fano-resonant photonic crystals, *Appl. Phys. Lett.* **106**, 181104 (2015).
 - [17] H. Li, M. Qin, L. Wang, X. Zhai, R. Ren, and J. Hu, Total absorption of light in monolayer transition-metal dichalcogenides by critical coupling, *Opt. Express* **25**, 31612 (2017).
 - [18] S. M. Bahauddin, H. Robotjazi, and I. Thomann, Broadband absorption engineering to enhance light

- absorption in monolayer MoS₂, *ACS Photonics* **3**, 853 (2016).
- [19] A. Sobhani, A. Lauchner, S. Najmaei, C. Ayala-Orozco, F. Wen, J. Lou, and N. J. Halas, Enhancing the photocurrent and photoluminescence of single crystal monolayer MoS₂ with resonant plasmonic nanoshells, *Appl. Phys. Lett.* **104**, 031112 (2014).
- [20] S. Butun, S. Tongay, and K. Aydin, Enhanced light emission from large-area monolayer MoS₂ using plasmonic nanodisc arrays, *Nano Lett.* **15**, 2700 (2015).
- [21] D. Zheng, S. Zhang, Q. Deng, M. Kang, P. Nordlander, and H. Xu, Manipulating coherent plasmon-exciton interaction in a single silver nanorod on monolayer WSe₂, *Nano Lett.* **17**, 3809 (2017).
- [22] J. Sun, H. Hu, D. Zheng, D. Zhang, Q. Deng, S. Zhang, and H. Xu, Light-emitting plexciton: Exploiting plasmon-exciton interaction in the intermediate coupling regime, *ACS Nano* **12**, 10393 (2018).
- [23] Y. Li, A. Chernikov, X. Zhang, A. Rigosi, H. M. Hill, A. M. van der Zande, and T. F. Heinz, Measurement of the optical dielectric function of monolayer transition-metal dichalcogenides: MoS₂, MoSe₂, WS₂, and WSe₂, *Phys. Rev. B* **90**, 205422 (2014).
- [24] A. R. Beal, W. Y. Liang, and H. P. Hughes, Kramers-Kronig analysis of the reflectivity spectra of 3R-WS₂ and 2H-WSe₂, *J. Phys. C: Solid State Phys.* **9**, 2449 (1976).
- [25] S. J. Kim, J. Park, M. Esfandyarpour, E. F. Pecora, P. G. Kik, and M. L. Brongersma, Superabsorbing, artificial metal films constructed from semiconductor nanoantennas, *Nano Lett.* **16**, 3801 (2016).
- [26] F. Hu, Y. Luan, M. E. Scott, J. Yan, D. G. Mandrus, X. Xu, and Z. Fei, Imaging exciton-polariton transport in MoSe₂ waveguides, *Nat. Photonics* **11**, 356 (2017).
- [27] R. Verre, D. G. Baranov, B. Munkhbat, J. Cuadra, M. Käll, and T. Shegai, Transition metal dichalcogenide nanodisks as high-index dielectric Mie nanoresonators, *Nat. Nanotechnol.* **14**, 679 (2019).
- [28] H. Zhang, B. Abhiraman, Q. Zhang, J. Miao, K. Jo, S. Roccasecca, M. W. Knight, A. R. Davoyan, and D. Jariwala, Hybrid exciton-plasmon-polaritons in van der Waals semiconductor gratings, *Nat. Commun.* **11**, 3552 (2020).
- [29] Q. Zhang, S. Dong, G. Cao, and G. Hu, Exciton polaritons in mixed-dimensional transition metal dichalcogenides heterostructures, *Opt. Lett.* **45**, 4140 (2020).
- [30] L. C. Botten, R. C. McPhedran, N. A. Nicorovici, and G. H. Derrick, Periodic models for thin optimal absorbers of electromagnetic radiation, *Phys. Rev. B* **55**, R16072 (1997).
- [31] J. M. Geffrin, B. Garcia-Camara, R. Gomez-Medina, P. Albella, L. S. Froufe-Perez, C. Eyraud, A. Litman, R. Vaillon, F. Gonzalez, M. Nieto-Vesperinas, J. J. Saenz, and F. Moreno, Magnetic and electric coherence in forward- and back-scattered electromagnetic waves by a single dielectric subwavelength sphere, *Nat. Commun.* **3**, 1171 (2012).
- [32] M. Decker, I. Staude, M. Falkner, J. Dominguez, D. N. Neshev, I. Brener, T. Pertsch, and Y. S. Kivshar, High-efficiency dielectric Huygens' surfaces, *Adv. Opt. Mater.* **3**, 813 (2015).
- [33] C. Liu, H. Ye, Y. Wang, Y. Sun, Y. Liu, Z. Yu, and L. Yu, Beyond dipole excitation: The performance of quadrupole-based Huygens' metasurface, *Opt. Lett.* **45**, 4847 (2020).
- [34] J. R. Piper, V. Liu, and S. Fan, Total absorption by degenerate critical coupling, *Appl. Phys. Lett.* **104**, 251110 (2014).
- [35] X. Ming, X. Liu, L. Sun, and W. J. Padilla, Degenerate critical coupling in all-dielectric metasurface absorbers, *Opt. Express* **25**, 24658 (2017).
- [36] J. Tian, Q. Li, P. A. Belov, R. K. Sinha, W. Qian, and M. Qiu, High-*Q* all-dielectric metasurface: Super and suppressed optical absorption, *ACS Photonics* **7**, 1436 (2020).
- [37] P. Chen, T. W. Lo, Y. Fan, S. Wang, H. Huang, and D. Lei, Chiral coupling of valley excitons and light through photonic spin-orbit interactions, *Adv. Opt. Mater.* **8**, 1901233 (2020).
- [38] W. Suh, Z. Wang, and S. Fan, Temporal coupled-mode theory and the presence of non-orthogonal modes in lossless multimode cavities, *IEEE J. Quantum Electron.* **40**, 1511 (2004).
- [39] H. Li, C. Ji, Y. Ren, J. Hu, M. Qin, and L. Wang, Investigation of multiband plasmonic metamaterial perfect absorbers based on graphene ribbons by the phase-coupled method, *Carbon* **141**, 481 (2019).
- [40] J. Yu, B. Ma, A. Ouyang, P. Ghosh, H. Luo, A. Pattanayak, S. Kaur, M. Qiu, P. Belov, and Q. Li, Dielectric super-absorbing metasurfaces via PT symmetry breaking, *Optica* **8**, 1290 (2021).
- [41] H. A. Haus, *Waves and Fields in Optoelectronics* (Prentice-Hall, Englewood Cliffs, NJ, 1984).
- [42] T. Kaelberer, V. A. Fedotov, N. Papasimakis, D. P. Tsai, and N. I. Zheludev, Toroidal dipolar response in a metamaterial, *Science* **330**, 1510 (2010).
- [43] Y. He, G. Guo, T. Feng, Y. Xu, and A. E. Miroshnichenko, Toroidal dipole bound states in the continuum, *Phys. Rev. B* **98**, 161112(R) (2018).
- [44] P. D. Terekhov, V. E. Babicheva, K. V. Baryshnikova, A. S. Shalin, A. Karabchevsky, and A. B. Evlyukhin, Multipole analysis of dielectric metasurfaces composed of nonspherical nanoparticles and lattice invisibility effect, *Phys. Rev. B* **99**, 045424 (2019).